Physics of Fluids ARTICLE scitation.org/journal/phf

The study of shallow water flow with bottom topography by high-order compact gas-kinetic scheme on unstructured mesh

Cite as: Phys. Fluids 33, 083613 (2021); doi: 10.1063/5.0060631
Submitted: 21 June 2021 · Accepted: 31 July 2021 ·
Published Online: 18 August 2021

Fengxiang Zhao (赵丰祥),[1] Jianping Gan (甘剑平),[2,3] and Kun Xu (徐昆)[1,2,3,4,a)]

AFFILIATIONS

[1]Department of Mechanical and Aerospace Engineering, Hong Kong University of Science and Technology, Clear Water Bay, Kowloon, Hong Kong
[2]Department of Mathematics, Hong Kong University of Science and Technology, Clear Water Bay, Kowloon, Hong Kong
[3]Center for Ocean Research in Hong Kong and Macau (CORE), Hong Kong University of Science and Technology, Clear Water Bay, Kowloon, Hong Kong
[4]Shenzhen Research Institute, Hong Kong University of Science and Technology, Shenzhen 518057, China

Note: This paper is part of the special topic, Tribute to Frank M. White on his 88th Anniversary.
[a)]**Author to whom correspondence should be addressed:** makxu@ust.hk

ABSTRACT

A well-balanced compact high-order gas-kinetic scheme (GKS) on unstructured mesh is first developed for solving the shallow water equations with source terms. The distinguishable feature of the finite volume GKS is that based on the gas-kinetic formulation, a time-accurate gas distribution function can be constructed, from which both the fluxes and the flow variables can be explicitly evaluated at the cell interface. As a result, besides the update of cell-averaged conservative variables, the cell-averaged slopes of the flow variables can be updated as well. Equipped with both flow variables and their slopes, a fourth-order compact spatial reconstruction on unstructured mesh can be obtained as the initial condition at the beginning of each time step. For the shallow water flow, in order to preserve the well-balanced property, the advection and the source terms in the flux function have to be balanced properly. The current compact GKS achieves high-order accuracy, keeps the well-balanced property, and has super-robustness in the simulation of bore waves. The scheme is used in the shallow water flow studies, such as dam breaking and bore wave propagation. In addition, the pollution transport, morphodynamics, and bottom friction in the shallow water flow have been included in the scheme. In the end, the water discharge in the Pearl River estuary and the dam-break experiment with movable bed topography have been simulated.

I. INTRODUCTION

The shallow water equations are applied in the study of large-scale ocean circulations and small-scale coastal channel flows, such as tsunamis, pollutant transport, tides, and dam-break problems. Many numerical schemes for shallow water equations have been constructed,[1–3] and most of them have second-order accuracy. In comparison with second-order methods, high-order schemes have great advantages and potentials to get accurate solutions and keep computational efficiency.[4–7] Due to the advantages of high-order methods, extensive effort has been spent on the development of high-order schemes in the past decades for shallow water equations.[4,8–11] Unstructured mesh has good adaptability to complex geometry. Therefore, the development of high-order schemes on unstructured mesh has attracted much attention in engineering applications. The construction of a high-order finite volume scheme on unstructured mesh is a challenge due to the use of a large stencil in the reconstruction.[12] Almost all high-order schemes for the shallow water equations on unstructured mesh are based on the discontinuous Galerkin (DG) formulation,[4,11,13] which were originally developed for the compressible gas dynamics.[14–16] The DG method updates the inner degrees of freedom (DOFs) from its weak formulations. For discontinuous flow, additional numerical treatments, such as identifying trouble cells and limiting procedure, have to be designed in the DG method.[17–20]

The second-order gas-kinetic schemes have been developed in the past decades for compressible flow simulations[21–24] and the shallow water equations.[3] Unified gas-kinetic schemes (UGKS) based on

the direct modeling methodology[24] for the rarefied and continuum flow simulations have also been developed.[25–29] The time-accurate solution at a cell interface in GKS not only provides the flux function but also cell interface values. As a result, the cell-averaged flow variables and their slopes can be directly updated in GKS. Therefore, compact stencils can be designed for the initial data reconstruction. There are advantages in using compact stencil in the reconstruction, such as remaining uniformly high-order accuracy without oscillations.[30,31] The simplified WENO reconstruction for compact GKS has been fully developed in Ref. 16, where the central ingredients are to construct several low order polynomials and to design smoothness indicators to adaptively assemble them to get a high-order one. The most recent effort is about the optimization of stencil selection and the design of weighting functions.[32–34] WENO schemes can achieve very high-order accuracy in the smooth region and maintain nonoscillatory property across shock waves.[35] The WENO scheme has been extended to unstructured mesh[36,37] and the algorithm is complicated in the determination of the optimal linear weights. The simplified WENO method is developed in Ref. 16 by combining the ENO and WENO approaches.[30,38] Based on the time-accurate cell interface evolution solution in GKS, another advantage is to implement the two-stage fourth-order (S_2O_4) temporal discretization for time evolution,[39,40] which can use less stages for the same order of accuracy in comparison with Runge–Kutta approach. The S_2O_4 method has been fully validated in the previous GKS.[41–44] Due to the use of only two reconstructions for the fourth-order time accuracy, the computational cost of the scheme can be much reduced. The temporal accuracy can be further improved using the multistage and multiderivative methods.[45] The compact high-order GKS has been developed for the Navier–Stokes solutions.[16,46] In this study, the scheme will be developed for the shallow water equations with source terms on unstructured mesh.

This paper is organized as follows: The GKS for shallow water equations will be introduced in Sec. II. Section III is about the well-balanced property of the scheme. The compact GKS for the shallow water equations is further equipped with the tracking of scalar transport in Sec. IV. Section V is about the compact high-order reconstruction on unstructured mesh. In Sec. VI, the shallow water flow will be studied in many cases from smooth flow to the dam-breaking problem. More complicated engineering applications are included in Sec. VII. Section VIII is the conclusion.

II. GAS-KINETIC SCHEME FOR SHALLOW WATER EQUATIONS

A. Shallow water equations and kinetic model equation

The shallow water equations can be written as

$$\frac{\partial \mathbf{W}}{\partial t}+\frac{\partial \mathbf{F}_1(\mathbf{W})}{\partial x}+\frac{\partial \mathbf{F}_2(\mathbf{W})}{\partial y}=\mathbf{S}(\mathbf{W}), \tag{1}$$

where

$$\mathbf{W}=\begin{pmatrix} h \\ hU \\ hV \end{pmatrix}, \quad \mathbf{F}_1=\begin{pmatrix} hU \\ hU^2+\frac{1}{2}Gh^2 \\ hUV \end{pmatrix}, \quad \mathbf{F}_2=\begin{pmatrix} hV \\ hUV \\ hV^2+\frac{1}{2}Gh^2 \end{pmatrix},$$

and

$$\mathbf{S}=\begin{pmatrix} 0 \\ -GB_x h \\ -GB_y h \end{pmatrix}.$$

In the above equations, $\mathbf{W}$ is the flow variable, and $\mathbf{F}_1$ and $\mathbf{F}_2$ are the corresponding fluxes in x and y directions. Source term $\mathbf{S}$ is coming from the bottom profile $\nabla_{\mathbf{x}}B(x,y)=(B_x,B_y)$, and G is the gravitational constant. The shallow water equations in Eq. (1) can be derived from the generalized BGK model with the inclusion of an acceleration term. The BGK model can be written as[3]

$$f_t+\mathbf{u}\cdot\nabla_{\mathbf{x}}f+\nabla\Phi\cdot\nabla_{\mathbf{u}}f=\frac{g-f}{\tau}, \tag{2}$$

where f is the distribution function with particle velocity $\mathbf{u}=(u,v)$ and g is the equilibrium state approached by f. τ is the relaxation time. $\nabla\Phi$ is the acceleration of particle due to external force from the bottom topography with $\nabla\Phi=-G\nabla_{\mathbf{x}}B$. The equilibrium state g is a Maxwellian distribution function,[3]

$$g=h\left(\frac{\lambda}{\pi}\right)e^{-\lambda(\mathbf{u}-\mathbf{U})^2}, \tag{3}$$

where λ is defined by $\lambda=1/Gh$. Due to the conservation in relaxation process from f to g, f, and g satisfy the compatibility condition,

$$\int\frac{g-f}{\tau}\boldsymbol{\psi}\mathrm{d}\Xi=\mathbf{0}, \tag{4}$$

where $\boldsymbol{\psi}=(\psi_1,\psi_2,\psi_3)^T=(1,u,v)^T$ and $\mathrm{d}\Xi=\mathrm{d}u\mathrm{d}v$. The macroscopic flow variables and their fluxes can be obtained from the distribution function f as

$$\mathbf{W}=\int f\boldsymbol{\psi}\mathrm{d}\Xi, \tag{5}$$

and

$$(\mathbf{F}_1,\mathbf{F}_2)^T=\int f\boldsymbol{\psi}\mathbf{u}\mathrm{d}\Xi. \tag{6}$$

The source term $\mathbf{S}$ can be obtained from the distribution function f as

$$\mathbf{S}=-\int\nabla\Phi\cdot\nabla_{\mathbf{u}}f\boldsymbol{\psi}\mathrm{d}\Xi. \tag{7}$$

The formal solution of the BGK model in Eq. (2) with external forcing term is

$$f(\mathbf{x},t,\mathbf{u})=\frac{1}{\tau}\int_0^t g(\mathbf{x}',t',\mathbf{u}')e^{-(t-t')/\tau}\mathrm{d}t'+e^{-t/\tau}f_0(\mathbf{x}_0,\mathbf{u}_0), \tag{8}$$

where $\mathbf{x}$ is the numerical quadrature point on the cell interface for flux evaluation, and $\mathbf{x}$ can be set as $(0,0)$ for simplicity in a local coordinate system with both normal and tangential directions as the x- and y-directions. The formal solution describes an evolution process for the distribution function. The trajectory of fluid particle is given by $\mathbf{x}=\mathbf{x}'+\mathbf{u}'(t-t')+\frac{1}{2}\nabla\Phi(t-t')^2$, and the velocity of the particle is $\mathbf{u}=\mathbf{u}'+\nabla\Phi(t-t')$. The acceleration on the particle trajectory has a second-order effect ($\sim t^2$), but it has the first-order contribution ($\sim t$) to the particle velocity.

B. Time evolution solution of GKS

The well-balanced GKS with second-order spatial and temporal accuracy was first developed in Ref. 3 on structured mesh. In a finite volume scheme, the solution update depends on the cell interface flux. Based on an initial linearly distributed flow variables on both sides of a cell interface, a time-accurate solution on the interface is obtained for the flux evaluation.[23] The initial distribution functions on both sides of a cell interface are defined as

$$f_0(\mathbf{x}',\mathbf{u}) = g^l(\mathbf{x},0,\mathbf{u})[1+\mathbf{a}^l\cdot\mathbf{x}'](1-H(x')), + g^r(\mathbf{x},0,\mathbf{u})[1+\mathbf{a}^r\cdot\mathbf{x}']H(x'), \tag{9}$$

where $g^k(\mathbf{x},0,\mathbf{u})$ is the Maxwellian distribution function, and $H(x')$ is the Heaviside function. $\mathbf{a}^k=(a_1^k,a_2^k)$ $(k=l,r)$ is the spatial derivative of g^k, and it is determined by the piecewise initial polynomials of flow variables. See Appendix A for the specific formula.

The formal solution $f_0(\mathbf{x}_0,\mathbf{u}_0)$ in Eq. (8) represents the particle-free transport from $(\mathbf{x}_0,0,\mathbf{u}_0)$ to $(\mathbf{x},t,\mathbf{u})$ under external force field. The f_0 is given by

$$f_0(\mathbf{x}_0,\mathbf{u}_0) = g^l(\mathbf{x},0,\mathbf{u}_0)[1-\mathbf{a}^l\cdot\mathbf{u}t]H(u), + g^r(\mathbf{x},0,\mathbf{u}_0)[1-\mathbf{a}^r\cdot\mathbf{u}t](1-H(u)).$$

The particle velocity $\mathbf{u}_0$ in the Maxwellian distribution $g^k(\mathbf{x},0,\mathbf{u}_0)$ is related to $\mathbf{u}$ through the relationship,

$$\begin{aligned} g^k(\mathbf{x},0,\mathbf{u}_0) &= g^k(\mathbf{x},0,\mathbf{u}) + \nabla_{\mathbf{u}}g^k(\mathbf{x},0,\mathbf{u})\cdot(\mathbf{u}_0-\mathbf{u}), \\ &= g^k(\mathbf{x},0,\mathbf{u})\left[1+2\lambda^k\nabla\Phi\cdot(\mathbf{u}-\mathbf{U})t\right]. \end{aligned} \tag{10}$$

The $f_0(\mathbf{x}_0,\mathbf{u}_0)$ in Eq. (8) becomes

$$\begin{aligned} f_0(\mathbf{x}_0,\mathbf{u}_0) = {} & g^l(\mathbf{x},0,\mathbf{u})\left[1+2\lambda^l\nabla\Phi\cdot(\mathbf{u}-\mathbf{U}^l)t-\mathbf{a}^l\cdot\mathbf{u}t\right]H(u), \\ & + g^r(\mathbf{x},0,\mathbf{u})\left[1+2\lambda^r\nabla\Phi\cdot(\mathbf{u}-\mathbf{U}^r)t-\mathbf{a}^r\cdot\mathbf{u}t\right] \\ & \times(1-H(u)). \end{aligned} \tag{11}$$

Similarly, the equilibrium state in the formal solution [Eq. (8)] can be approximated as

$$g(\mathbf{x}',t',\mathbf{u}') = \bar{g}(\mathbf{x},0,\mathbf{u})\left[1+2\bar{\lambda}\nabla\Phi\cdot(\mathbf{u}-\mathbf{U})(t-t') -\bar{\mathbf{a}}\cdot\mathbf{u}(t-t')+\bar{A}t'\right], \tag{12}$$

where $\bar{\mathbf{a}}$ and $\bar{A}$ are the spatial and temporal derivatives of the equilibrium state. Based on the modeling of f_0 and g, the time accurate distribution function f at a cell interface in GKS is[3]

$$\begin{aligned} & f(\mathbf{x},t,\mathbf{u}) \\ & = \bar{g}(\mathbf{x},0,\mathbf{u})\left[C_1+C_2(\bar{\mathbf{a}}^l\cdot\mathbf{u}H(u)+\bar{\mathbf{a}}^r\cdot\mathbf{u}(1-H(u)))+C_3\bar{A}\right], \\ & + C_2\bar{g}(\mathbf{x},0,\mathbf{u})\left[-2\alpha_{k,m}\bar{\lambda}(\nabla\Phi^lH(u)+\nabla\Phi^r(1-H(u)))\cdot(\mathbf{u}-\bar{\mathbf{U}})\right], \\ & + C_4\left[g^l(\mathbf{x},0,\mathbf{u})H(u)+g^r(\mathbf{x},0,\mathbf{u})(1-H(u))\right], \\ & + C_5g^l(\mathbf{x},0,\mathbf{u})\left[\mathbf{a}^l\cdot\mathbf{u}-2\alpha_{k,m}\lambda^l\nabla\Phi^l\cdot(\mathbf{u}-\mathbf{U}^l)\right]H(u), \\ & + C_5g^r(\mathbf{x},0,\mathbf{u})\left[\mathbf{a}^r\cdot\mathbf{u}-2\alpha_{k,m}\lambda^r\nabla\Phi^r\cdot(\mathbf{u}-\mathbf{U}^r)\right](1-H(u)), \end{aligned} \tag{13}$$

where $\alpha_{k,m}$ $(k=1,2,\ m=1,2,3)$ are constants for a well-balanced scheme, which will be given in Sec. III. The coefficients C_i $(i=1,2,\ldots,5)$ are

$$C_1 = 1-e^{-t/\tau},\quad C_2 = -\tau(1-e^{-t/\tau})+te^{-t/\tau},$$
$$C_3 = -\tau(1-e^{-t/\tau})+t,\quad C_4 = e^{-t/\tau},\quad C_5 = -te^{-t/\tau}.$$

The fluxes at the cell interface can be obtained by taking the moments of the gas distribution function and the total transport of mass and momentum within a time step can be further integrated in time. More detailed formulation can be found in Ref. 23.

III. WELL-BALANCED HIGH-ORDER GKS

A. High-order discretization

Taking moments on Eq. (1), the flow variables in a cell Ω_j is updated by

$$\frac{\partial\mathbf{W}_j}{\partial t} = -\frac{1}{|\Omega_j|}\int_{\partial\Omega_j}\mathbf{F}\cdot\mathbf{n}dl+\frac{1}{|\Omega_j|}\int\int_{\Omega_j}\mathbf{S}d\Omega_j, \tag{14}$$

where $\mathbf{W}_j$ is the cell-averaged flow variable, $\mathbf{F}=(\mathbf{F}_1,\mathbf{F}_2)$ is the time-dependent flux at cell interface, which can be obtained from the moments of the gas distribution function in Eq. (13). The $\mathbf{W}_j$ is defined as

$$\mathbf{W}_j \equiv \frac{1}{|\Omega_j|}\int\int_{\Omega_j}\mathbf{W}(\mathbf{x})d\Omega. \tag{15}$$

The line integral of the flux in Eq. (14) can be discretized by a q-point Gaussian quadrature formula,

$$\begin{aligned} -\frac{1}{|\Omega_j|}\int_{\partial\Omega_j}\mathbf{F}\cdot\mathbf{n}dl &= -\frac{1}{|\Omega_j|}\sum_{l=1}^{l_0}\left(|\Gamma_l|\sum_{k=1}^{q}\omega_k\mathbf{F}(\mathbf{x}_k)\cdot\mathbf{n}_l\right), \\ &\equiv \mathcal{L}_j^F(\mathbf{W}), \end{aligned} \tag{16}$$

where $|\Gamma_l|$ is the side length of the cell, l_0 is the total number of cell sides, such as $l_0=3$ for a triangular mesh, $\mathbf{n}_l$ is the unit outer normal vector, and q and ω_k are the total number of integration points and weight of the Gaussian integration formula. In order to evaluate the above numerical flux, the initial data $\mathbf{W}(\mathbf{x}_k)$ is reconstructed using the compact spatial stencil, which are presented in Sec. V. For a linearly distributed bottom profile, ∇B is a local constant vector. The cell averaged $\mathbf{S}$ becomes

$$\begin{aligned} \frac{1}{|\Omega_j|}\int\int_{\Omega_j}\mathbf{S}d\Omega_j &= h_j(0,-GB_{j,x},-GB_{j,y})^T, \\ &\equiv \mathcal{L}_j^S(\mathbf{W}), \end{aligned} \tag{17}$$

where h_j is the cell average of h in Ω_j. Based on Eq. (14), the high-order GKS updates the solutions using S2O4 temporal discretization,[39,40]

$$\begin{aligned} \mathbf{W}_j^{n+1/2} &= \mathbf{W}_j^n+\frac{1}{2}\Delta t\mathcal{L}_j(\mathbf{W}^n)+\frac{1}{8}\Delta t^2\frac{\partial}{\partial t}\mathcal{L}_j(\mathbf{W}^n), \\ \mathbf{W}_j^{n+1} &= \mathbf{W}_j^n+\Delta t\mathcal{L}_j(\mathbf{W}^n)+\frac{1}{6}\Delta t^2\left(\frac{\partial}{\partial t}\mathcal{L}_j(\mathbf{W}^n)+2\frac{\partial}{\partial t}\mathcal{L}_j(\mathbf{W}^{n+1/2})\right), \end{aligned} \tag{18}$$

where $\mathcal{L}_j=\mathcal{L}_j^F+\mathcal{L}_j^S$.

B. Well-balanced property

The fully discretized scheme in Eq. (18) is a well-balanced method once it keeps the steady state solution $U = V = 0$ and $h + B = Const$. For a well-balanced scheme, the flux transport and the external forcing on the left-hand side of Eq. (2) have to be precisely balanced, and it is required to balance the flux transport and external forcing in the discrete form of Eq. (13). Based on the balance requirement, the coefficients $\alpha_{k,m}$ in Eq. (13) can be fully determined.[3]

Define the terms related to advection and acceleration in Eq. (13) as

$$L(g) \equiv g\left[\mathbf{a}^l \cdot \mathbf{u}H(u) + \mathbf{a}^r \cdot \mathbf{u}(1 - H(u))\right] + g\left[-2\alpha_{k,m}\lambda(\nabla\Phi^l H(u) + \nabla\Phi^r(1 - H(u))) \cdot (\mathbf{u} - \mathbf{U})\right]. \tag{19}$$

The well-balanced condition becomes

$$\int L(g)\boldsymbol{\psi} \mathrm{d}\Xi = \mathbf{0}, \quad \int L(g)\boldsymbol{\psi} u \mathrm{d}\Xi = \mathbf{0}. \tag{20}$$

In triangular mesh, the river bottom profile is discretized by connecting the bottom heights on three nodes of the cell. Thus, the normal derivatives of the bottom profiles become discontinuous at neighboring cells, and the tangential derivatives are continuous. As a result, $L(g)$ can be simplified as

$$L(g) = g\left[a_1^l \cdot uH(u) + a_1^r \cdot u(1 - H(u))\right] + g\left[-2\alpha_{1,m}\lambda(\Phi_x^l H(u) + \Phi_x^r(1 - H(u))) \cdot (u - U)\right] + ga_2 \cdot v + g\left[-2\alpha_{2,m}\lambda\Phi_y \cdot (v - V)\right]. \tag{21}$$

Here $\alpha_{k,m}$ depends on the moments ψ_m together with $L(g)$ shown in Eq. (20). The coefficients can be determined by the condition in Eq. (20) as

$$\alpha_{1,1} = \frac{3}{4}, \quad \alpha_{1,2} = 1, \quad \alpha_{1,3} = \frac{5}{4}; \quad \alpha_{2,m} = 1.$$

The detailed derivation is given in Appendix B. In a well-balanced state, the solution of the distribution function in Eq. (13) with $\tau = 0$ becomes

$$f(\mathbf{x}, t, \mathbf{u}) = g^e(\mathbf{x}, 0, \mathbf{u})(1 + tA^e) = g^e(\mathbf{x}, 0, \mathbf{u}),$$

where a constant flow variable is kept at the cell interface.

It can be shown that the high-order discretization can keep the steady state as well. Without loss of generality, the discretized equations for the momentum update in Eq. (18) become

$$\begin{aligned}(hU)_j^{n+1/2} &= (hU)_j^n + \frac{1}{2}\Delta t(L_j^2)^n + \frac{1}{8}\Delta t^2 \frac{\partial}{\partial t}(\mathcal{L}_j^2)^n, \\ (hU)_j^{n+1} &= (hU)_j^n + \Delta t(L_j^2)^n \\ &\quad + \frac{1}{6}\Delta t^2\left(\frac{\partial}{\partial t}(\mathcal{L}_j^2)^n + 2\frac{\partial}{\partial t}(\mathcal{L}_j^2)^{n+1/2}\right),\end{aligned} \tag{22}$$

where $(L_j^2)^n = (\mathcal{L}_j^{F,2})^n + (\mathcal{L}_j^{S,2})^n$. Based on the numerical flux at cell interface, the calculation of $\mathcal{L}_j^{F,2}$ in Eq. (16) can be done on a standard triangle $\tilde{\Omega}_j$ with three nodes $(0, 0)$, $(1, 0)$, and $(0, 1)$ and gives

$$\begin{aligned}\mathcal{L}_j^{F,2} &= -\frac{1}{|\tilde{\Omega}_j|}\sum_{l=1}^{3}\left(|\tilde{\Gamma}_l|\sum_{k=1}^{2}\frac{1}{4}Gh^2\tilde{n}_{l,x}\right) \\ &= -Gh_{j,x}h_j = GB_{j,x}h_j,\end{aligned} \tag{23}$$

which is exactly balanced with the source term

$$\mathcal{L}_j^{S,2} = -GB_{j,x}h_j. \tag{24}$$

In addition, the time derivative $\partial(L_j^2)^n/\partial t$ and $\partial(L_j^2)^{n+1/2}/\partial t$ will always be zero due to the balanced evolution solution given in Eq. (20). Note that Eq. (23) holds only if $h + B$ is constant at each quadrature point of the cell interface after reconstruction, which is satisfied using surface gradient reconstruction method.[2]

IV. GKS FOR SCALAR TRANSPORT

In order to capture the pollution propagation in the shallow water flow, the scalar transport equation has to be solved in GKS as well. For the GKS with scalar transport, a new distribution function is constructed and satisfies the same BGK model as the shallow water flow,

$$f_t^s + \mathbf{u} \cdot \nabla_{\mathbf{x}} f^s + \nabla\Phi \cdot \nabla_{\mathbf{u}} f^s = \frac{g^s - f^s}{\tau}, \tag{25}$$

where g^s is the distribution function of equilibrium state. The g^s is defined as

$$\begin{aligned}g^s &= h\left(\frac{\lambda}{\pi}\right)^{3/2} e^{-\lambda((\mathbf{u}-\mathbf{U})^2 + (z-Z)^2)} \\ &= \left(\frac{\lambda}{\pi}\right)^{1/2} e^{-\lambda(z-Z)^2} g,\end{aligned} \tag{26}$$

where g is the Maxwellian distribution function in Eq. (3), and Z is the scalar function recovered microscopically by z. From the BGK model, the scalar transport equation can be derived as

$$\frac{\partial(hZ)}{\partial t} + \frac{\partial(hZU)}{\partial x} + \frac{\partial(hZV)}{\partial y} = 0. \tag{27}$$

Based on the BGK model in Eq. (25), similar to Eq. (13), the solution of f^s is given by

$$\begin{aligned}f^s(\mathbf{x}, t, \mathbf{u}, z) &= \bar{g}^s(\mathbf{x}, 0, \mathbf{u})\left[C_1 + C_2(\bar{\mathbf{a}}^{s,l} \cdot \mathbf{u}H(u) + \bar{\mathbf{a}}^{s,r} \cdot \mathbf{u}(1 - H(u))) + C_3\bar{A}^s\right], \\ &\quad + C_2\bar{g}^s(\mathbf{x}, 0, \mathbf{u})\left[-2\alpha_{k,m}\bar{\lambda}(\nabla\Phi^l H(u) + \nabla\Phi^r(1 - H(u))) \cdot (\mathbf{u} - \bar{\mathbf{U}})\right] \\ &\quad + C_4\left[g^{s,l}(\mathbf{x}, 0, \mathbf{u})H(u) + g^{s,r}(\mathbf{x}, 0, \mathbf{u})(1 - H(u))\right] \\ &\quad + C_5 g^{s,l}(\mathbf{x}, 0, \mathbf{u})\left[\mathbf{a}^{s,l} \cdot \mathbf{u} - 2\alpha_{k,m}\lambda^l\nabla\Phi^l \cdot (\mathbf{u} - \mathbf{U}^l)\right]H(u) \\ &\quad + C_5 g^{s,r}(\mathbf{x}, 0, \mathbf{u})\left[\mathbf{a}^{s,r} \cdot \mathbf{u} - 2\alpha_{k,m}\lambda^r\nabla\Phi^r \cdot (\mathbf{u} - \mathbf{U}^r)\right](1 - H(u)).\end{aligned} \tag{28}$$

The derivatives of distribution function, i.e., $\mathbf{a}^{s,k}$ $(k = l, r)$, are coming from the derivatives of $g^s = g_1 g$. Let $g_1 = (\lambda/\pi)^{1/2} e^{-\lambda(z-Z)^2}$, the derivative of g^s can be obtained as

$$\frac{\partial g^s}{\partial w} = \frac{\partial g_1}{\partial w} g + g_1 \frac{\partial g}{\partial w},$$

where $\partial g/\partial w$ is the same as that in Sec. II and $\partial g_1/\partial w$ can be obtained similarly as given in Appendix C. Then, based on the above distribution function for the coupled system, the flux for hZ in Eq. (27) can be obtained.

V. OVERVIEW OF COMPACT HIGH-ORDER RECONSTRUCTION

In Secs. II and IV, the time-accurate solution for the distribution function at a cell interface is presented. The solution depends on the initial condition, which needs to be reconstructed on unstructured mesh. Based on the cell averaged values and their slopes of flow variables, the compact fourth-order reconstruction is presented in Ref. 16. The time-accurate flow variables are required in the compact reconstruction. Based on the time-accurate solution of the distribution function in Eqs. (13) or (28), the flow variables and their time derivatives can be explicitly evaluated at a cell interface,

$$\begin{aligned}\mathbf{W}^n(\mathbf{x}) &= \int \widehat{f}(t^n)\boldsymbol{\psi}\mathrm{d}\Xi,\\ \mathbf{W}_t^n(\mathbf{x}) &= \int \widehat{f}_t(t^n)\boldsymbol{\psi}\mathrm{d}\Xi,\end{aligned} \tag{29}$$

where $\widehat{f}(t^n)$ and $\widehat{f}_t(t^n)$ are the zero-order and first-order terms of the linear approximation to f in Eq. (13). The purpose of the linear approximation is to give an evolution solution of f that is determined by $\widehat{f}(t^n)$ and $\widehat{f}_t(t^n)$ and equivalent to the original f in Eq. (13) in the sense of time integration. See Ref. 16 for the details. For a high-order scheme, the cell interface values can be updated in two steps,

$$\begin{aligned}\mathbf{W}^{n+1/2}(\mathbf{x}) &= \mathbf{W}^n(\mathbf{x}) + \frac{1}{2}\Delta t\mathbf{W}_t^n(\mathbf{x}),\\ \mathbf{W}^{n+1}(\mathbf{x}) &= \mathbf{W}^n(\mathbf{x}) + \Delta t\mathbf{W}_t^{n+1/2}(\mathbf{x}),\end{aligned} \tag{30}$$

where $\mathbf{W}_t^{n+1/2}(\mathbf{x})$ can be obtained in the same way as $\mathbf{W}_t^n(\mathbf{x})$ at the middle stage. Then, the cell-averaged derivatives of flow variables at t^{n+1} can be evaluated from $\mathbf{W}^{n+1}(\mathbf{x})$ by Gauss's law,

$$\begin{aligned}\mathbf{W}_{j,x}^{n+1} &\equiv \frac{1}{|\Omega_j|}\int\int_{\Omega_j}\frac{\partial \mathbf{W}^{n+1}(x,y)}{\partial x}dxdy = \frac{1}{|\Omega_j|}\int_{\partial\Omega_j}\mathbf{W}^{n+1}(x,y)dy,\\ \mathbf{W}_{j,y}^{n+1} &\equiv \frac{1}{|\Omega_j|}\int\int_{\Omega_j}\frac{\partial \mathbf{W}^{n+1}(x,y)}{\partial y}dxdy = -\frac{1}{|\Omega_j|}\int_{\partial\Omega_j}\mathbf{W}^{n+1}(x,y)dx.\end{aligned} \tag{31}$$

The numerical quadrature points can be used in the evaluation of interface integration,

$$\begin{aligned}\mathbf{W}_{j,x}^{n+1} &= \frac{1}{|\Omega_j|}\sum_{l=1}^{l_0}\left(|\Gamma_l|\cdot n_{l,x}\sum_{k=1}^{q}\omega_k\mathbf{W}^{n+1}(\mathbf{x}_k)\right),\\ \mathbf{W}_{j,y}^{n+1} &= \frac{1}{|\Omega_j|}\sum_{l=1}^{l_0}\left(|\Gamma_l|\cdot n_{l,y}\sum_{k=1}^{q}\omega_k\mathbf{W}^{n+1}(\mathbf{x}_k)\right),\end{aligned} \tag{32}$$

where $n_{l,x}$ and $n_{l,y}$ are the two components of the unit outer normal vector on the lth interface of cell Ω_j.

With the updates of cell averaged flow variables and their $x-$ and $y-$direction derivatives in each cell, the stencils used for reconstruction are shown in Fig. 1, which involves the physical domain of dependence of the target cell within a time step. A class of compact high-order reconstruction from fourth to sixth order of accuracy has been developed in Ref. 16. The nonlinear compact reconstruction is used for the determination nonequilibrium state of the gas distribution function and an evolved smooth reconstruction for the equilibrium state. The detailed formulation of nonlinear compact reconstruction is given in Ref. 16. In the current reconstruction, in order to have a well-balanced property, the surface gradient method is used.[2] Especially, the variable $h(x,y)+B(x,y)$ is used in the reconstruction instead of $h(x, y)$. The flow chart of the overall compact GKS is presented in Fig. 2.

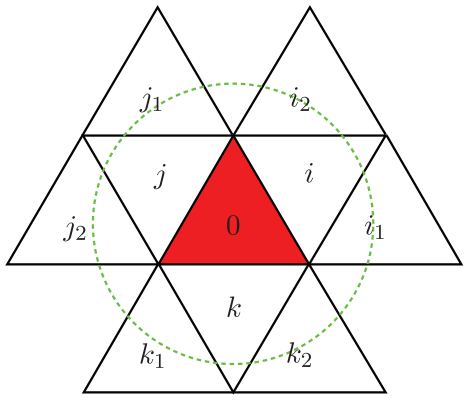

FIG. 1. A schematic of reconstruction stencil of compact GKS. The green dotted circle is a schematic of the physical domain of dependence, that is, at a definite time step, the fluid element in cell 0 may interact with the fluid element in the range of the circle. In each cell of the stencil, three data, i.e., one cell averages and two cell-averaged derivatives, are known.

A summary of the nonlinear fourth-order compact reconstruction will be given here. The formula of the compact reconstruction is a nonlinear combination of the lower-order and high-order polynomials, i.e., the so-called combination of ENO and WENO methodology. The candidate stencils for the nonlinear reconstruction are given as follows:

$$\begin{aligned}S_0 &= \{Q_0, Q_i, Q_j, Q_k, Q_{i_1}, Q_{i_2}, Q_{j_1}, Q_{j_2}, Q_{k_1}, Q_{k_2}, \nabla Q_0, \nabla Q_i, \nabla Q_j, \nabla Q_k\},\\ S_1 &= \{Q_0, Q_i, Q_{i_1}, Q_{i_2}, Q_j, \nabla Q_i\}, \quad S_2 = \{Q_0, Q_i, Q_{i_1}, Q_{i_2}, Q_k, \nabla Q_i\},\\ S_3 &= \{Q_0, Q_j, Q_{j_1}, Q_{j_2}, Q_k, \nabla Q_j\}, \quad S_4 = \{Q_0, Q_j, Q_{j_1}, Q_{j_2}, Q_i, \nabla Q_j\},\\ S_5 &= \{Q_0, Q_k, Q_{k_1}, Q_{k_2}, Q_i, \nabla Q_k\}, \quad S_6 = \{Q_0, Q_k, Q_{k_1}, Q_{k_2}, Q_j, \nabla Q_k\},\\ S_7 &= \{Q_0, Q_i, Q_j, Q_k\}.\end{aligned}$$

A cubic polynomial $P(\mathbf{x})$ can be determined by S_0, six quadratic polynomials $q_k(\mathbf{x})$ $(k = 1, 2, \ldots, 6)$ can be determined by S_k, and a linear polynomial $q_7(\mathbf{x})$ can be determined by S_7. The least squares method is used to determine these candidate polynomials and the details can be found in Ref. 16. The polynomial of the nonlinear fourth-order compact reconstruction is

$$R(\mathbf{x}) = \sum_{k=1}^{n} w_k q_k(\mathbf{x}) + w_0\left(\frac{1+C}{C}P(\mathbf{x}) - \sum_{k=1}^{n}\frac{C_k}{C}q_k(\mathbf{x})\right). \tag{33}$$

The nonlinear weights w_k are

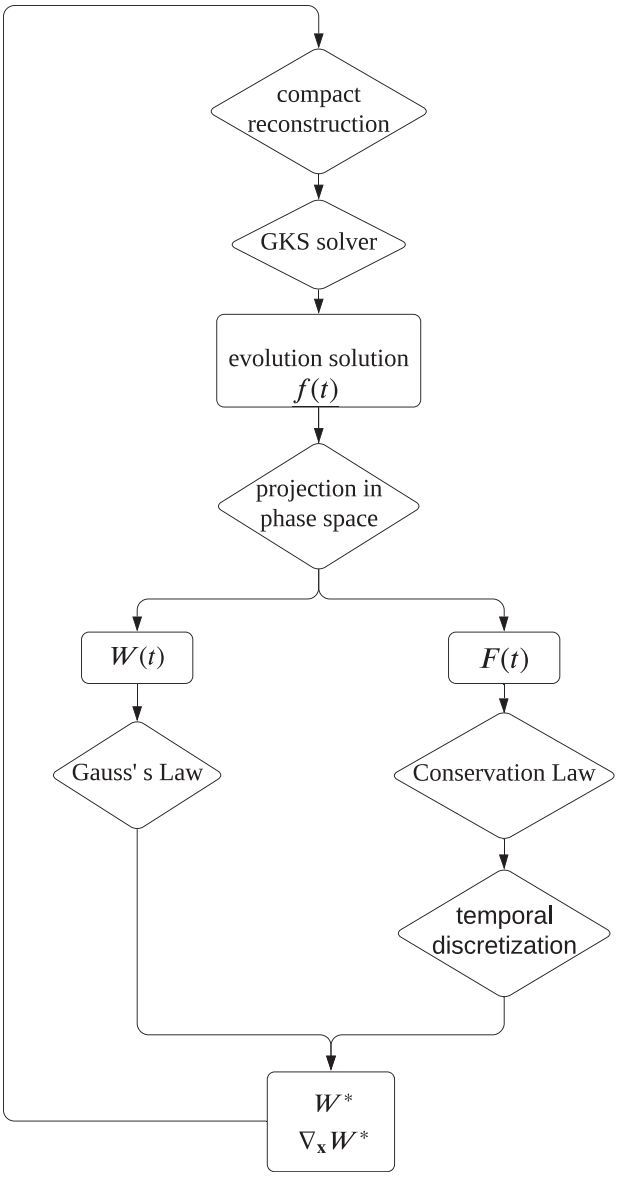

FIG. 2. Flow chart of the compact GKS. The evolution solution $f(t)$ of GKS is given by Eq. (13). The projection in phase space is defined by Eqs. (5) and (6). W^* is the cell-averaged value at $t = t^*$. The detailed algorithm of compact reconstruction can refer to.[16] The core of the compact GKS is to implement the high-order spatial reconstruction and temporal discretization by using the time-accurate evolution solution provided by the GKS solver.

$$w_k = \frac{\tilde{w}_k}{\sum_{j=0}^{n} \tilde{w}_j}, \qquad \tilde{w}_k = \bar{d}_k \left(1 + \left(\frac{\tau_Z}{IS_k + \epsilon}\right)^3\right), \tag{34}$$

and the linear weights $\bar{d}_k$ are

$$\bar{d}_0 = \frac{C}{1+C}, \quad \bar{d}_k = \frac{C_k}{1+C}, \quad k = 1, \ldots, n, \tag{35}$$

where ϵ is a small positive number with a value 1×10^{-8} for all numerical tests in this paper, n is the number of the substencils, and τ_Z is the local higher-order reference value to indicate smoothness of the large stencil given by IS_k,[33] and it is given as

$$\tau_Z = \sum_{l=1}^{3} |2IS_0 - IS_{2l-1} - IS_{2l}|.$$

Coefficients C and C_k are required to satisfy

$$\sum_{k=1}^{k=n} C_k = 1, \quad C > 0.$$

In this paper, $C_k = 1/n = 1/7$.

VI. STUDY OF SHALLOW WATER FLOWS

The compact high-order GKS will be used in shallow water flow studies. The time step used in the computation is mostly determined by the CFL condition with $CFL = 0.4$. The gravitational acceleration is taken as $G = 9.812$ if not specified. The collision time τ for inviscid flow at a cell interface is defined by

$$\tau = \varepsilon \Delta t + C_{num} \left| \frac{h_l^2 - h_r^2}{h_l^2 + h_r^2} \right| \Delta t,$$

where $\varepsilon = 0.05$, $C_{num} = 5$, and h_l^2 and h_r^2 are the pressures at the left and right sides of a cell interface. The reason for including the pressure jump term in the relaxation time is to enhance the artificial dissipation in the case of bore waves.

A. Well-balanced property

The well-balanced property of the compact GKS on unstructured mesh is validated by a numerical test. The initial condition is a two-dimensional steady state solution with nonflat bottom topography. The bottom topography is

$$B(x, y) = 0.8 e^{-50\left[(x-1)^2 + (y-1)^2\right]},$$

and the steady state is

$$h = 1 - B(x, y), \quad U = 0, \quad V = 0.$$

The computational domain is taken as $[0, 2] \times [0, 2]$, and the triangular mesh with cell size $h_{mesh} = 0.05$ is used. The gravitational acceleration is taken as $G = 1.0$. The discretized bottom topography is shown in Fig. 3. The errors of flow variables at $t = 0.1$ and $t = 10$ are listed in Table I. The error remains at the same level at different computational output time.

B. Shock tube problems

The 1D shock tube problem is simulated over flat and nonflat bottom topography on 2D unstructured mesh. First, the case with a flat bottom topography is tested, i.e., $B(x, y) = 0$. The initial condition is

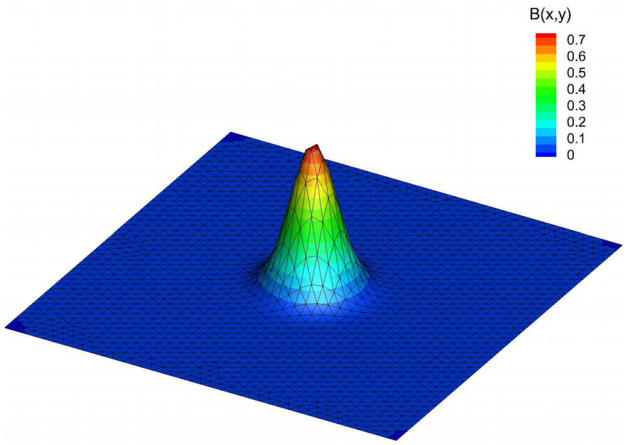

FIG. 3. Well-balanced property study: The bottom profile and a coarse mesh with cell size $h_{mesh} = 0.05$.

$$(h, U, V) = \begin{cases} (1, 0, 0), & 0 \le x < 0.5, \\ (h_R, 0, 0), & 0.5 \le x \le 1, \end{cases}$$

where two h_R of $h_R = 1 \times 10^{-1}$ and $h_R = 1 \times 10^{-3}$ are employed. The intensity of shock and expansion wave in the shock tube problem depends on the ratio of initial water depths of upstream and downstream. The gravitational acceleration is set to be $G = 1.0$. The computational domain is $[0, 1] \times [0, 0.5]$, and the cell size of the triangular mesh is $h_{mesh} = 0.01$. In addition, in order to verify the scheme for the coupled scheme with scalar transport, the scalar transport simulation is included in the weak case. The initial condition of scalar is set to

$$Z = \begin{cases} Z_l, & 0 \le x < 0.5, \\ Z_r, & 0.5 \le x \le 1, \end{cases}$$

TABLE I. The errors of flow variables of the solutions obtained by compact GKS on triangular mesh with $h_{mesh} = 0.05$ at $t = 0.1$ and $t = 10$.

Time	$Error_{L^1}(h)$	$Error_{L^1}(hU)$	$Error_{L^1}(hV)$
t = 0.1	1.5531×10^{-11}	1.8835×10^{-11}	1.8992×10^{-11}
t = 10	4.0065×10^{-11}	2.1097×10^{-12}	1.1030×10^{-12}

where $(Z_l, Z_r) = (1 \times 10^{-5}, 0)$ and $(Z_l, Z_r) = (0, 1 \times 10^{-5})$ are taken, respectively. The reflecting boundary condition is imposed in the y-direction. The free boundary condition is used on the left and right boundaries.

The results from compact GKS are shown in Figs. 4 and 5. Figure 5 is the distributions of h and hU along the horizontal centerline. The current scheme presents high-resolution solution in the rarefaction and shock waves. The results of scalar transport are shown in Fig. 6, where the water separated by the initial diaphragm is located on both sides of the contact discontinuity wave.

Next, the transcritical and subcritical flows in a channel are classical problems for the shallow water equations. Since the transcritical cases are more difficult, we only include two cases of transcritical flows here. The simulation channel is set as $[0, 25] \times [0, 2.5]$. The bottom topography is given by[3]

$$B(x, y) = \begin{cases} 0.2 - 0.05(x - 10)^2, & 8 \le x \le 12, \\ 0, & \text{otherwise}. \end{cases}$$

For the transcritical case without a shock wave, a discharge $hU = 1.53$ is imposed as the upstream boundary condition, and $h = 0.66$ is imposed as the downstream boundary condition in the subcritical case. For the transcritical flow with a shock wave, the discharge has a value $hU = 0.18$ at the upstream boundary and $h = 0.33$ is imposed as the downstream boundary condition.

The simulation results are given in Fig. 7. The water surface $h + B$ and discharge hU along the horizontal centerline are extracted

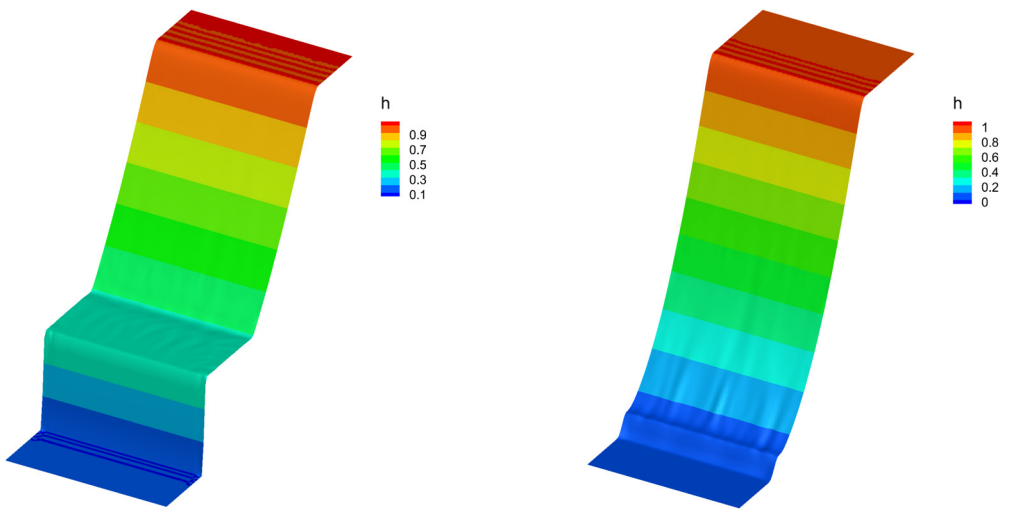

FIG. 4. One-dimensional dam-break problem with a flat bottom topography. The 3D contour distributions of water surface for the both cases at $t = 0.3$ (left) and $t = 0.2$ (right), respectively. The cell size is $h_{mesh} = 1/100$.

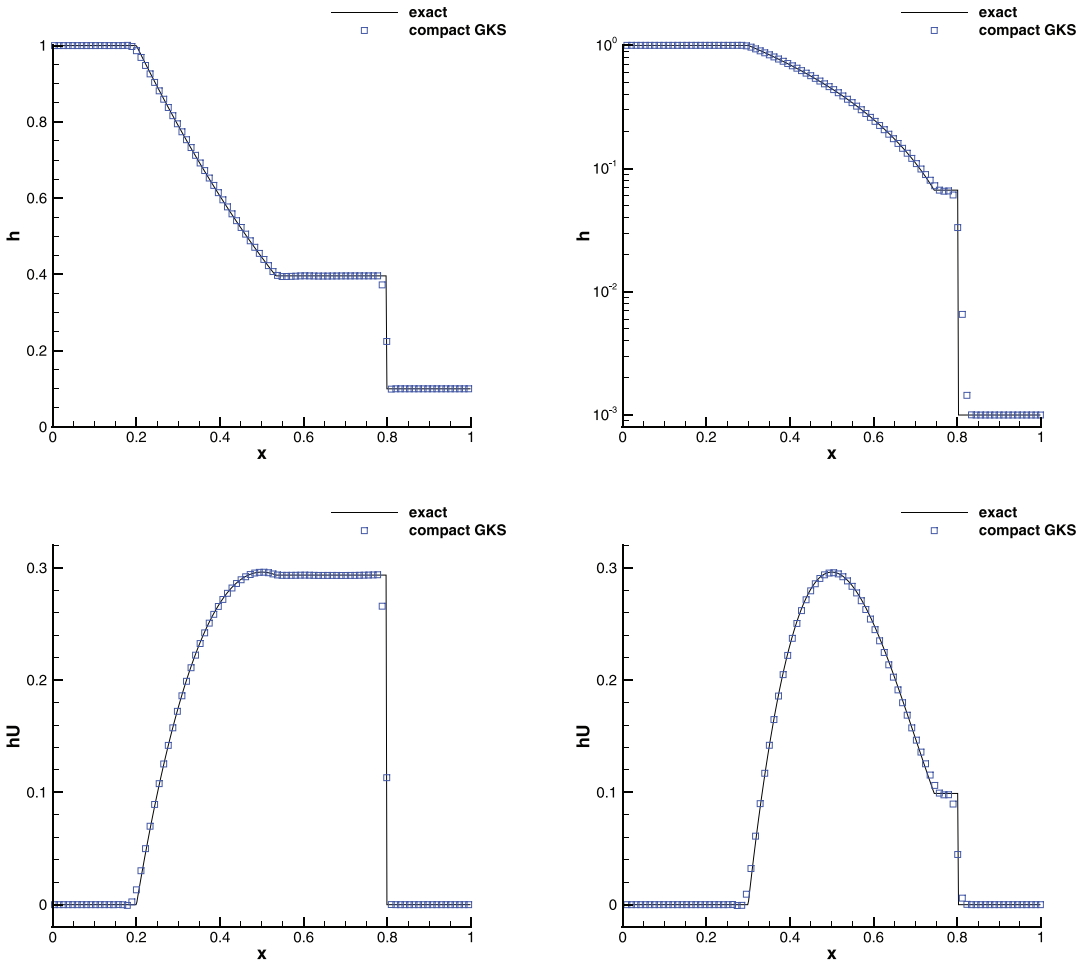

FIG. 5. One-dimensional shock tube problem with a flat bottom topography. The water surface and discharge along the horizontal centerline of the computational domain for the both cases at $t = 0.3$ (left) and $t = 0.2$ (right), respectively. The cell size is $h_{mesh} = 1/100$.

from 2D simulation on unstructured mesh. The reference solution is obtained by refining the mesh five times. Accurate solutions have been obtained. The solutions from the 2D GKS are as accurate as those from 1D calculation, such as the 1D DG scheme.[9] The L_1 error of hU of the current results is about 1.97×10^{-4} for the first case and 7.55×10^{-3} for the second case, respectively.

C. Two-dimensional dam-break problem

The 2D dam-break problem is studied as that in Refs. 10 and 47. Figure 8 shows the computational domain and mesh with local enlargement. The length of the dam breach is 75 and it starts at $y = 95$. The dam itself has a width of 10 and its left side is located at $x = 95$. At $t = 0$ the still water surface has a discontinuity with $h_l = 10$ and $h_r = \epsilon$ on both sides of the breach, and two values of $\epsilon = 5$ and $\epsilon = 1 \times 10^{-3}$ are used to simulate the wet bed and dry bed cases, respectively. The initial condition of scalar Z is set as

$$Z(x, y) = \begin{cases} 1, & x \le x_Z, \\ 0, & \text{otherwise}, \end{cases}$$

where $x_Z = 90$ for the wet bed case and $x_Z = 95$ for the dry bed case. The boundary condition on the far right is the free boundary, and the other boundary conditions are the nonpenetration slip wall boundaries. The mesh size far from the breach is $h_{mesh} = 2.5$ and is locally refined by 3.3 times around the dam breach.

The 3D water surface heights at $t = 7.2$ are shown in Fig. 9. The discontinuous bore waves are captured without spurious oscillations. The contours of water surface and "pollutant" species hZ are plotted in Fig. 10. It clearly shows that the wave propagating speed is higher in the dry bed case. Compared with the results of the second-order scheme in Ref. 47, the current solution presents more detailed flow structures. In addition, the unevenness of the locations of scalar variable is due to difference in the initial interface location.

D. Flow in the Pearl River estuary

The computational domain in the Pearl River estuary is approximately given in Fig. 11, where the real bottom topography is artificially generated. The estuary and the mesh in the computation are shown in Fig. 11, where the Lantao and Hong Kong islands are included. The

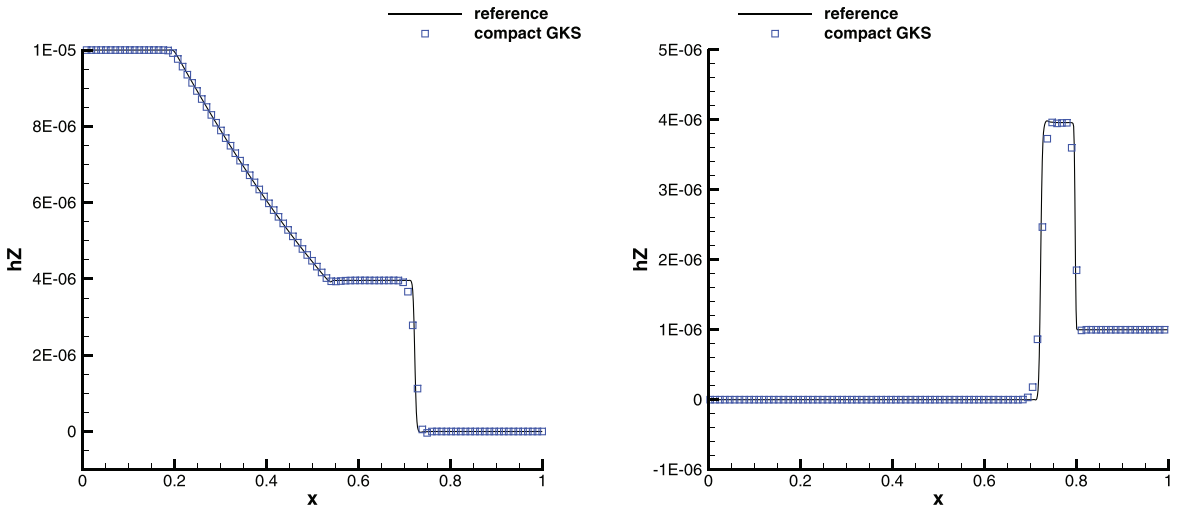

FIG. 6. Scalar transport in a shock tube. The distributions of hZ along the horizontal centerline at $t = 0.3$ of the weak discontinuity. The left corresponds to $Z_l = 1 \times 10^{-5}, Z_r = 0$, and the right corresponds to $Z_l = 0, Z_r = 1 \times 10^{-5}$. The cell size of triangular mesh is $h_{mesh} = 0.01$.

mesh size is $h_{mesh} = 20$, and there are 5871 triangular cells in total. In the Pearl River estuary, four river inlets (inlet 1, inlet 2, inlet 3, and inlet 4) and one river outlet (outlet) are included. Along the clockwise direction, the boundary from point A to B in the domain is set to be outlet boundary condition with a fixed water surface height. At the narrowest river channel, there is only one mesh cell. The discharges at the four inlets are set to 0.002, 0.003, 0.003, and 0.001. The water surface height at the boundary from point A to B is set as $0.33 - B(x, y)$. The outlet boundary condition is also adopted in the one river outlet. The no-penetration slip wall boundary condition is set at other boundaries. The computational time is $t = 4.4 \times 10^5$, and the fully developed flow at the estuary is obtained. The pollutant is added in the inlet 2 from $t = 10\,000$. In Fig. 12, the streamline and discharge distribution at the final time are given. Figure 13 presents the distribution of Z at the final time. As shown in the result, the pollutants seem to concentrate on the north part of the Lantao island.

VII. SHALLOW WATER STUDY WITH ADDITIONAL REALISTIC MODELS

In the previous studies, the shallow water equations are only coupled with scalar transport. In this section, the models related to the movable bed and bottom friction will be added to the numerical scheme.

A. Bottom friction

The bottom friction effect is added to the shallow water equations,

$$\frac{\partial \mathbf{W}}{\partial t} + \frac{\partial \mathbf{F}_1(\mathbf{W})}{\partial x} + \frac{\partial \mathbf{F}_2(\mathbf{W})}{\partial y} = \mathbf{S}(\mathbf{W}) + \mathbf{S}_\tau(\mathbf{W}), \tag{36}$$

where $\mathbf{W}$, $\mathbf{F}_1$, $\mathbf{F}_2$, and $\mathbf{S}$ are same as those in Eq. (1). $\mathbf{S}_\tau(\mathbf{W})$ is the source term from bottom friction,

$$\mathbf{S}_\tau(\mathbf{W}) = \left(0, -\frac{\tau_{Bx}}{\rho}, -\frac{\tau_{By}}{\rho}\right)^T,$$

where τ_{Bx} and τ_{By} are the shear stress in the x and y directions, and ρ is the density of water. Here, a widely used friction formulation, i.e., the so-called Manning's law, is used to define the shear stress,[48]

$$\tau_{Bx} = \rho G h \frac{n_M^2 U \sqrt{U^2 + V^2}}{h^{4/3}},$$
$$\tau_{By} = \rho G h \frac{n_M^2 V \sqrt{U^2 + V^2}}{h^{4/3}},$$

where n_M is the Manning roughness coefficient. As a result, for the above equations, the corresponding BGK model becomes

$$f_t + \mathbf{u} \cdot \nabla_{\mathbf{x}} f + (\nabla \Phi + \nabla \Phi_\tau) \cdot \nabla_{\mathbf{u}} f = \frac{g - f}{\tau}, \tag{37}$$

where $\nabla \Phi_\tau$ term is added to recover $\mathbf{S}_\tau$. Based on the relationship between the kinetic model and the macroscopic equations, $\nabla \Phi_\tau$ can be expressed as

$$\nabla \Phi_\tau = \frac{1}{h}(S_\tau^{(1)}, S_\tau^{(2)}), \tag{38}$$

where $S_\tau^{(1)}$ and $S_\tau^{(2)}$ are the second and third terms of $\mathbf{S}_\tau$. The compact GKS of Eq. (36) can be obtained similarly as the previous one by replacing the acceleration term in Eq. (13) with the terms $\nabla \Phi + \nabla \Phi_\tau$. The other difference is to add the source term $\mathbf{S}_\tau$ contribution in Eq. (36) through

$$\frac{1}{|\Omega_j|} \int\int_{\Omega_j} \mathbf{S}_\tau \mathrm{d}x\mathrm{d}y.$$

B. Bottom morphodynamic model

Sediment transport can cause a change of bottom topography, such as bed-load, suspended-load, and wash-load transport. Here, only the bed-load transport is considered for sediment particles slide, roll, and saltate due to shear forces from the surrounding fluid close to

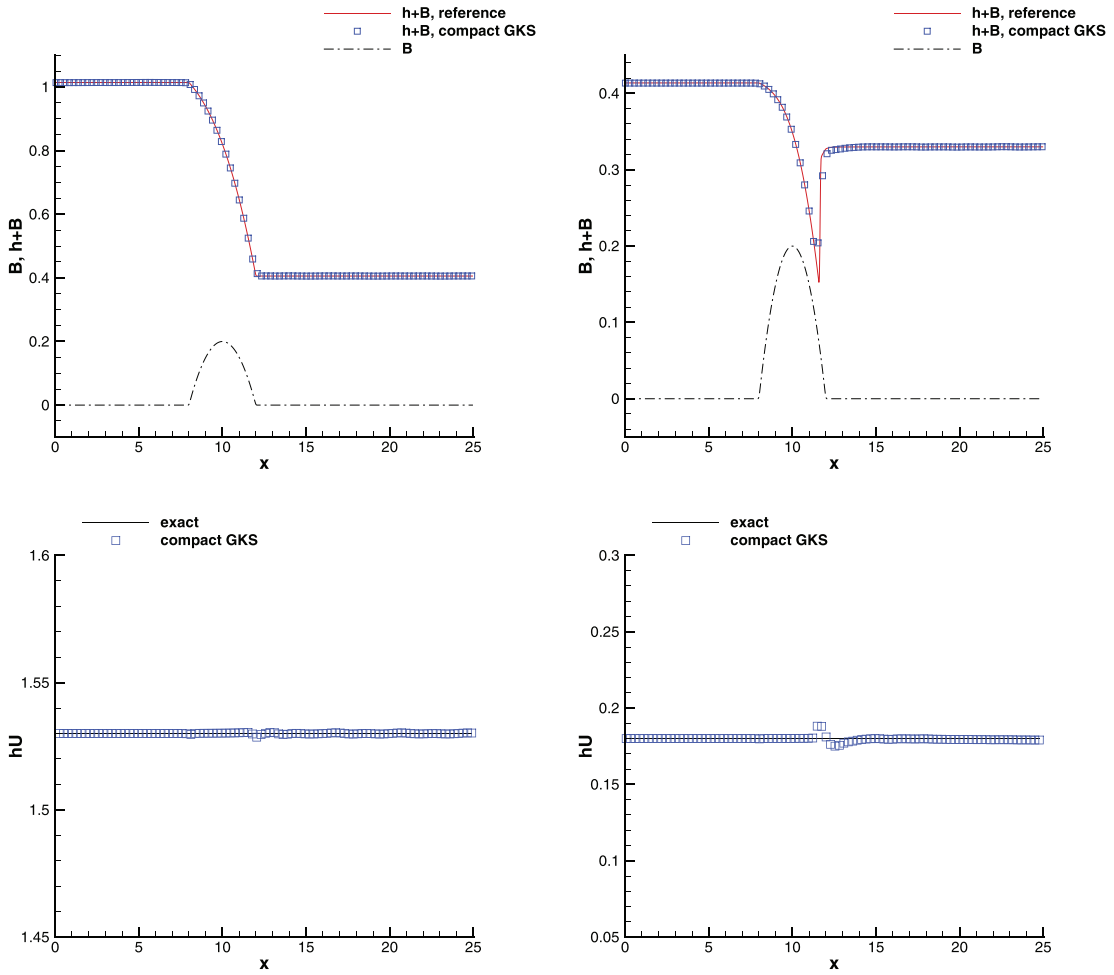

FIG. 7. Steady transcritical flow over a hump. The water surface $h + B$ and discharge hU distributions along the horizontal centerline for the cases without (left) and with (right) shock waves.

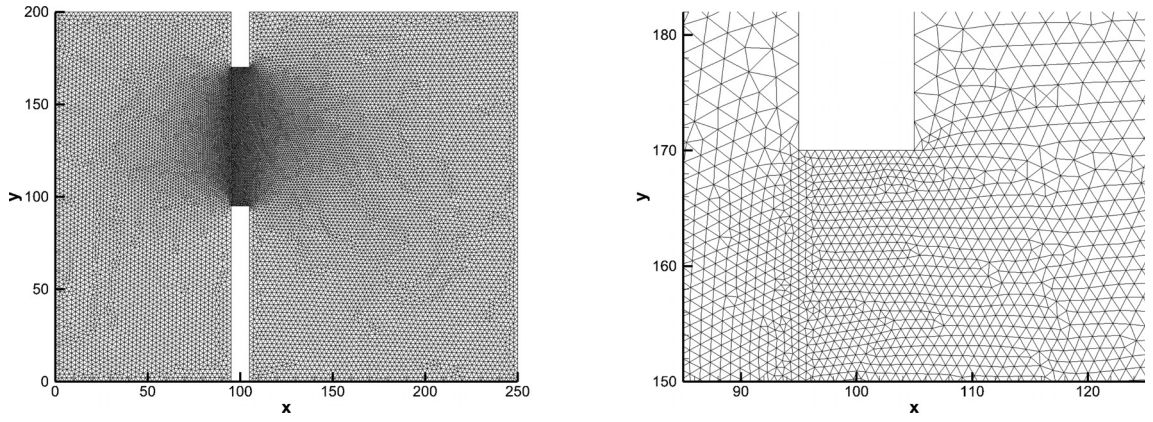

FIG. 8. Two-dimensional dam-break problem. The left is the computational domain and mesh, and the right is the enlarged view of the mesh around the dam breach. The mesh size far from the dam is $h_{mesh} = 2.5$ and is refined by 3.3 times in the dam breach area.

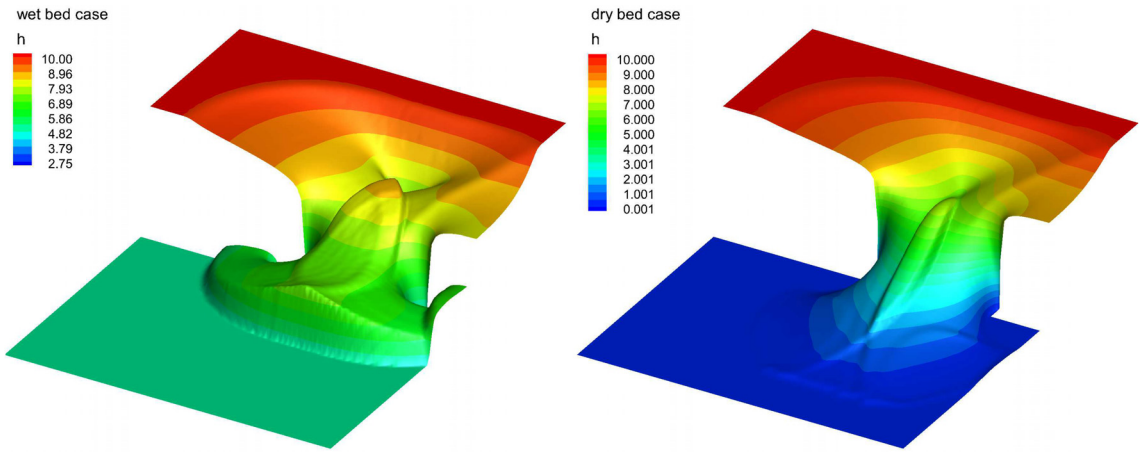

FIG. 9. Two-dimensional dam-break problem. Water height contours of wet bed case (left) and dry bed case (right) at $t = 7.2$.

the bottom.[49] The topographic evolution is modeled by the sediment continuity Exner equation,[49]

$$\frac{\partial B(\mathbf{x}, t)}{\partial t} + \eta \nabla \cdot \mathbf{Q}_B = 0, \tag{39}$$

where $\eta = 1/(1-p)$ and p is the material porosity. The direction of the flux is taken as the same direction as the water flow velocity, and the $\mathbf{Q}_B$ is given as

$$\mathbf{Q}_B = |\mathbf{Q}_B| \mathbf{n}_\mathbf{U},$$

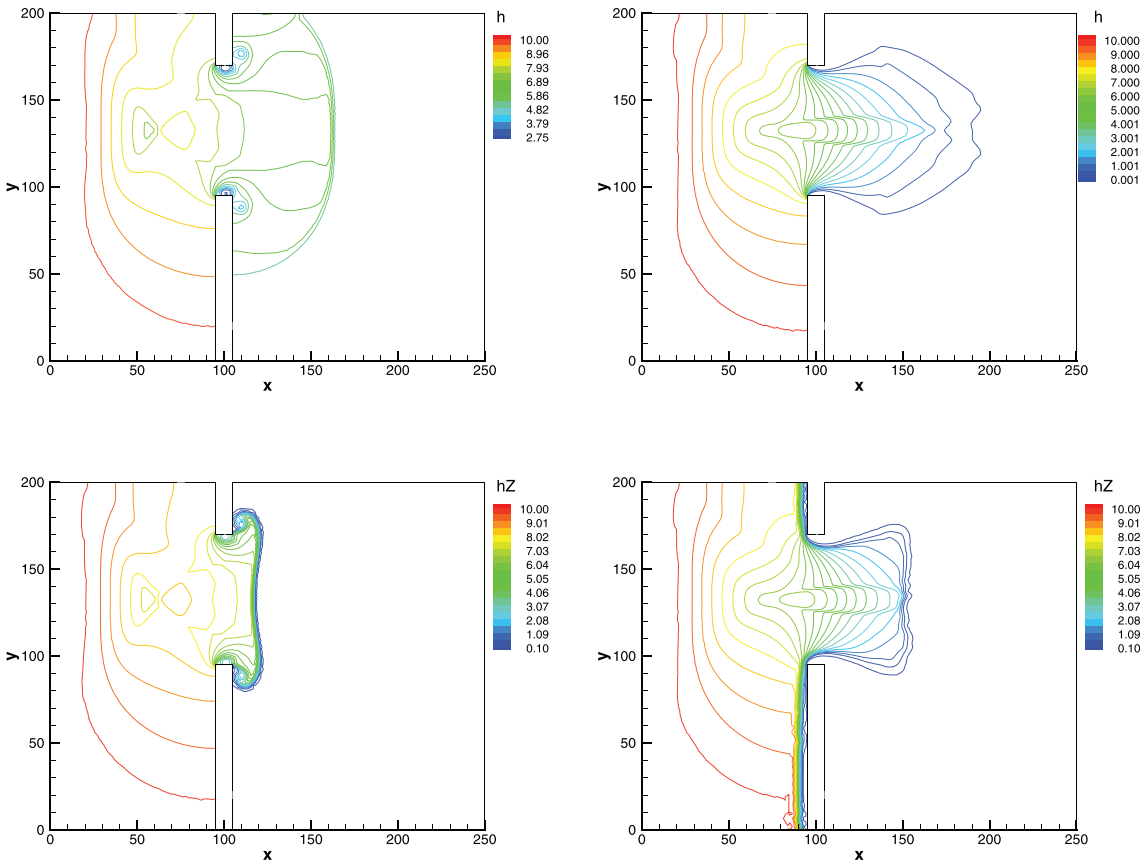

FIG. 10. Two-dimensional dam-break problem. Discharge contours of wet bed case (left) and dry bed case (right) at $t = 7.2$.

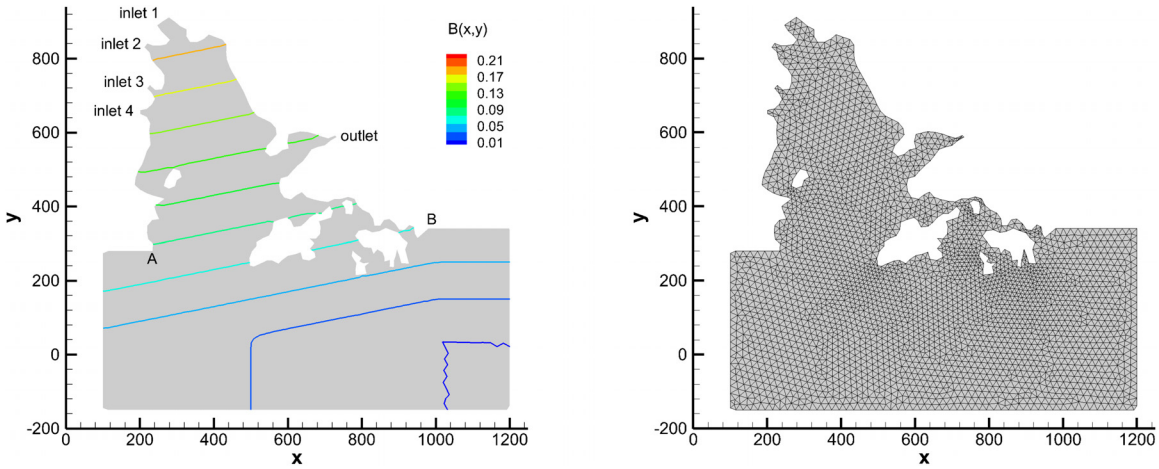

FIG. 11. Flow in the Pearl River estuary. The bottom topography (left) and the computational mesh (right). The mesh size is $h_{mesh} = 20$, and there are 5871 cells in total.

where $\mathbf{n}_U$ is the unit flow velocity vector, and $|\mathbf{Q}_B|$ is the magnitude of the sediment flux. Many empirical models have been proposed for $|\mathbf{Q}_B|$. In this paper, the Meyer-Peter and Mueller model is used,[48]

$$|\mathbf{Q}_B| = \sqrt{G(s-1)d_m^3}\,8(\theta-\theta_c)^{3/2}, \quad \theta > \theta_c$$
$$\theta = \frac{n_M^2}{(s-1)d_m h^{1/3}}(U^2+V^2),$$

where θ_c is the dimensionless critical stress, and the model is effective when $\theta > \theta_c$.

The semidiscrete scheme for Eq. (39) is

$$\frac{\partial B_j}{\partial t} = -\frac{\eta}{|\Omega_j|}\sum_{l=1}^{l_0}|\Gamma_l|\left(\sum_{k=1}^{q}\omega_k(|\mathbf{Q}_B|\mathbf{n}_\mathbf{u})(\mathbf{x}_k)\cdot\mathbf{n}_l\right). \tag{40}$$

For the case of shallow water flow with a movable bottom, the system becomes Eqs. (36) and (39). First, the shallow water equations Eq. (36) is solved by compact GKS, and the time-accurate evolution solution of flow variables $\mathbf{W}$ at cell interface is known. Then, the sediment flux $\mathbf{Q}_B$ can be directly evaluated, and B_j is updated by the two-step Runge–Kutta method,

$$B_j^{n+1/2} = B_j^n + \frac{1}{2}\Delta t\mathcal{L}_j^B(\mathbf{W}^n),$$
$$B_j^{n+1} = B_j^n + \Delta t\mathcal{L}_j^B(\mathbf{W}^{n+1/2}),$$

where $\mathcal{L}_j^B(\mathbf{W}^n)$ is the RHS of Eq. (40) with $t = t^n$. After updating B_j, the linear bottom topography in each cell can be reconstructed from their values in the cell Ω_j and three neighboring cells.

C. Dam-break flow over a movable bed

Equipped with movable bed and bed friction in the shallow water model, a realistic dam-break flow over movable bed is simulated. The experiment study of the case was given in Ref. 51, and the numerical simulations have been done previously from different schemes.[50,52] The sketch of the experiment of the dam-break flow over a movable bed is shown in Fig. 14. There is a flume with a length of 6 m, the upstream width of the

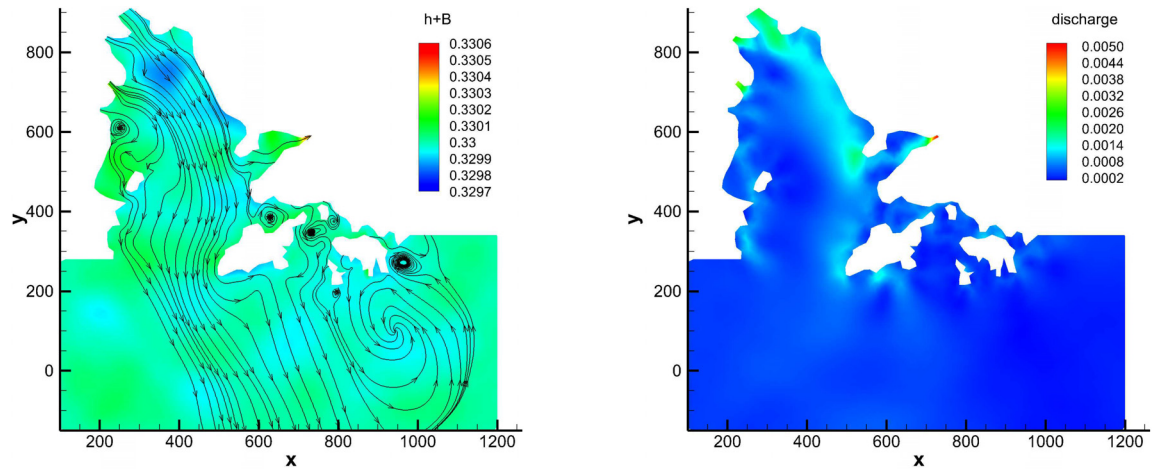

FIG. 12. Flow in the Pearl River estuary. The left is the streamline in the estuary. The right is the discharge in the estuary.

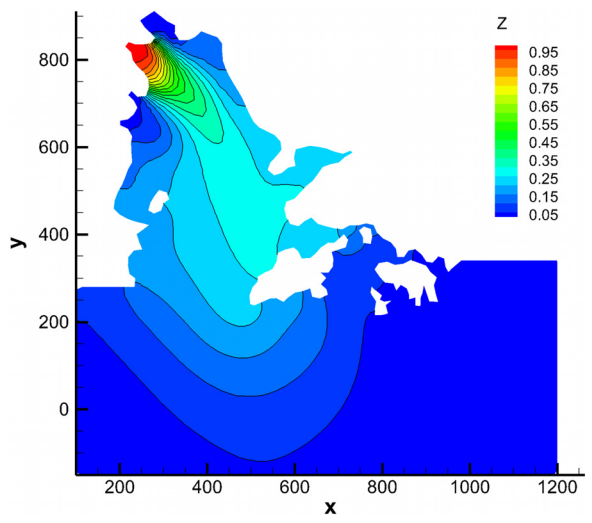

FIG. 13. Flow in the Pearl River estuary. The distribution contours of Z at the computational time $t = 4.4 \times 10^5$.

flume is 0.25 m, and it suddenly expands to 0.5 m at $x = 4$ m. A dam in the flume is placed at $x = 3$ m. Four measurement points are located at $P1(4.2, 0.125)$, $P2(4.95, 0.125)$, $P3(4.2, 0.375)$, and $P4(4.95, 0.375)$ to gauge the water surface height. The bed profiles at two cross sections, Sc1 ($x = 4.1$) and Sc2 ($x = 4.4$), were also measured.

Initially, the entire bottom of the flume is covered with a coarse and almost uniform sand with a thickness of 0.1 m. The sand has a median diameter of $d_m = 1.72$ mm, a specific density of $s = 2.63$, and a porosity of $p = 0.39$.[50] The Manning roughness coefficient takes $n_M = 0.026$, and the dimensionless critical stress takes $\theta_c = 0.047$.[50] The stationary water with a 0.25 m depth is stored in the flume on the upstream side of the dam, and the downstream of the dam is a dry area. The dam is broken at $t = 0$. The dam-breaking flow induces sand transport at the bottom of the flume. The boundary condition on the far right is the free boundary, and the other boundary conditions are no-penetration slip wall boundaries. Two meshes are used in the computation, and there are a total of 2112 cells in the coarse mesh, and a total of 7818 cells in the fine mesh. A local enlarged view of the coarse mesh is given in Fig. 14, where the mesh is refined at the dam.

The water surface height at four measured points is given in Fig. 15, and the experimental results are from.[52] Compared with

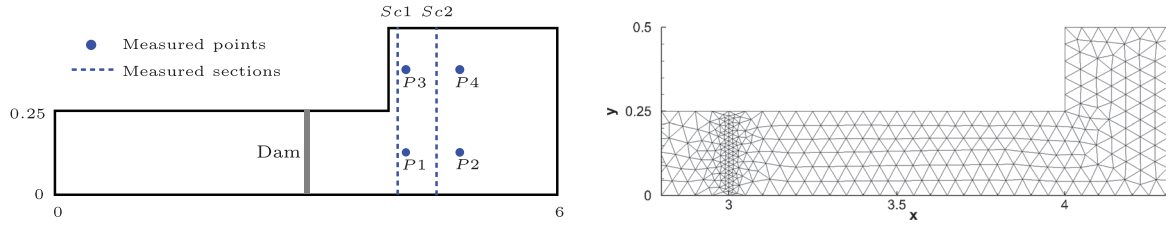

FIG. 14. Dam-break flow over movable bed. The left figure is the sketch of a dam-break flow experiment over a mobile bed. The right is the computational mesh with a local refinement.

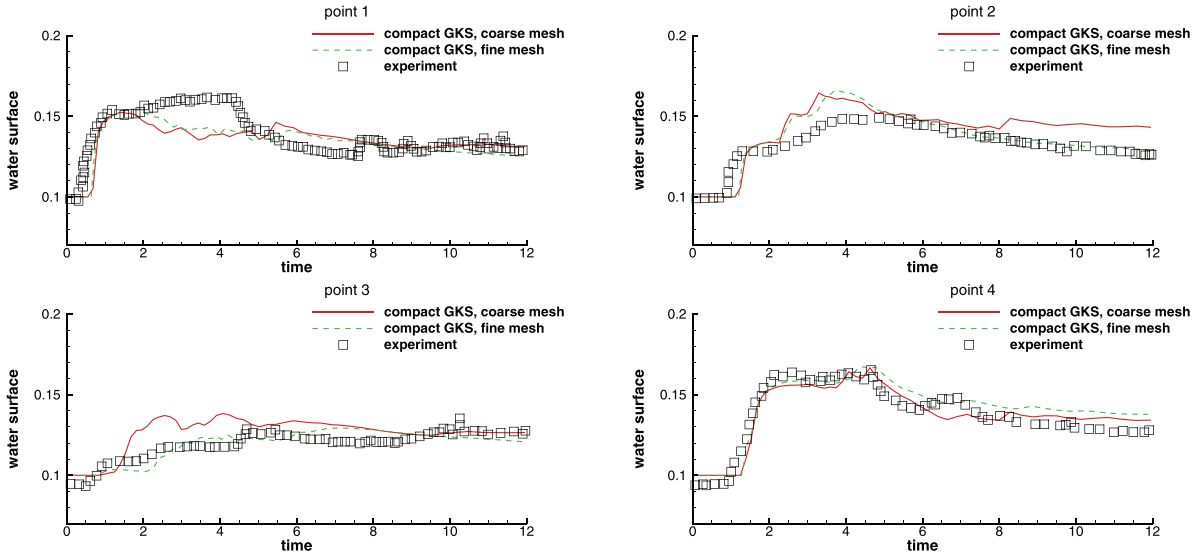

FIG. 15. Dam-break flow over movable bed. Water surface height of numerical and experimental results at different measured points.

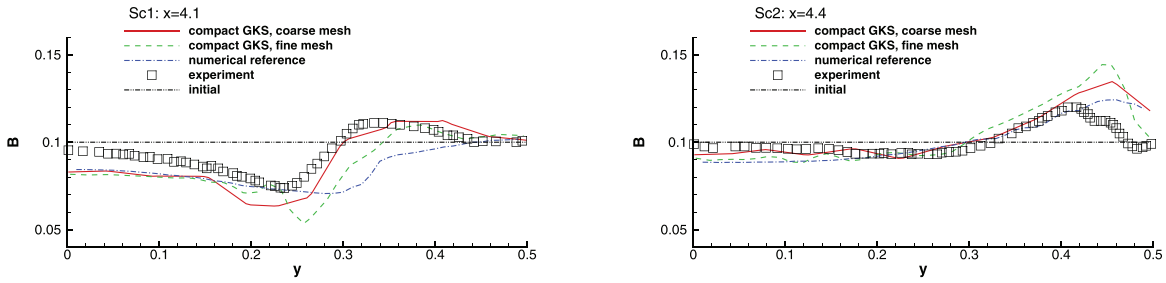

FIG. 16. Dam-break flow over movable bed. Bed profiles of numerical and experimental results at different measured sections. The numerical reference is the computational solution from.[50]

experimental data, the current simulation solutions are acceptable, except for relatively large deviations at point 1 in the time interval $2.0\ \mathrm{s} < t < 4.5\ \mathrm{s}$. The results on the fine mesh are better than those on the coarse mesh. Compared with the simulation results from the same mathematical model in Ref. 50, the current scheme seems to present more accurate solution at later time, such as $t > 5\,s$. Figure 16 shows the bed topography at two cross sections. The experimental and numerical results of[50] are also plotted as a reference. Compared with the solutions in Ref. 50, the results from the current compact GKS have a better match with the experimental measurements. The reason for the deviation between numerical simulation and experimental results may be that the mathematical model of sediment transport is not accurate enough in the specific flow area in the flume.

VIII. CONCLUSION

In this paper, for the shallow water flow, a well-balanced compact high-order GKS is presented. The distinguishable features of the current scheme are the following. A time-accurate evolution solution at the cell interface is constructed in the gas-kinetic scheme with the inclusion of particle acceleration due to the no-flat bottom topography. The time evolution solution at the cell interface not only provides numerical fluxes across the cell interface but also evolves the flow variables. As a result, both cell averaged flow variables and their slopes inside each control volume can be updated directly. Equipped with the flow variables and their gradients, a WENO-type high-order compact reconstruction can be designed on unstructured mesh. At the same time, due to the time-accurate fluxes, an efficient temporal discretization with the two stages and fourth-order method can be adopted. The compact high-order GKS is used in the studies of a wide range of shallow water flow problems with continuous and discontinuous solutions on unstructured mesh. High-order accuracy and strong robustness of the scheme have been confirmed. In order to simulate realistic flow problem, additional models are included in the system, such as scalar transport equation for pollutant propagation, Manning's formula for taking into account the friction effect from the river bottom, and the morphodynamics equation for following deformable river bottom from bed-load transport. The water flow in the Pearl River estuary and dam-break experiments are simulated.

ACKNOWLEDGMENTS

This research was supported by CORE as a Joint Research Centre for Ocean Research between QNLM and HKUST through Project No. QNLM20SC01-A, and the National Science Foundation of China Nos. 11772281 and 91852114.

APPENDIX: EXPANSIONS AND MOMENTS OF EQUILIBRIUM STATE

In the GKS, moments of an equilibrium gas distribution function need to be evaluated. The general moments of a Maxwellian distribution function with bound and unbounded integration limits are given in Ref. 23. Here, the moments of the Maxwellian specific to the shallow water equations will be listed. At the same time, the formulas to determine the modified coefficients in the distribution function for preserving the well-balanced property are presented.

APPENDIX A: DERIVATIVES OF AN EQUILIBRIUM DISTRIBUTION

For shallow water equations, the equilibrium distribution in Eq. (3) is a Maxwellian given by

$$g = h\left(\frac{\lambda}{\pi}\right) e^{-\lambda(\mathbf{u}-\mathbf{U})^2}.$$

Its first-order spatial and temporal derivatives are

$$\frac{\partial g}{\partial w} = ag, \quad a = \sum_{m=1}^{m=4} a_m \psi_m, \tag{A1}$$

where w refers to x, y, or t, and ψ_m takes $\psi_1 = 1, \psi_2 = u, \psi_3 = v$, and $\psi_4 = u^2 + v^2$. The coefficients a_m are fully determined from the derivatives of macroscopic flow variables, such as h, hU, and hV,

$$\begin{aligned} a_1 &= 3\lambda(U^2+V^2)\frac{h_w}{h} - 2\lambda\left(U\frac{(hU)_w}{h} + V\frac{(hV)_w}{h}\right), \\ a_2 &= 2\lambda\left(\frac{(hU)_w}{h} - 2U\frac{h_w}{h}\right), \\ a_3 &= 2\lambda\left(\frac{(hV)_w}{h} - 2V\frac{h_w}{h}\right), \\ a_4 &= \lambda\frac{h_w}{h}. \end{aligned} \tag{A2}$$

APPENDIX B: MODIFIED COEFFICIENTS IN THE GAS DISTRIBUTION FUNCTION FOR A WELL-BALANCED SCHEME

In Sec. III B, time-accurate evolution solution is given. For preserving a well-balanced steady state solution, the advection and

acceleration terms in evolution solution f should be balanced with the source term. Equation (20) in Sec. III B gives the mathematical constraints for a balanced evolution solution. The determination of the coefficients $\alpha_{k,m}$ ($k = 1, 2, m = 1, 2, 3$) is the following. For simplicity, define

$$\begin{aligned} L_{1,1}(g) &= a_1^l \cdot uH(u) + a_1^r \cdot u(1 - H(u)), \\ L_{1,2}(g) &= -2\alpha_{1,m}\lambda(\Phi_x^l H(u) + \Phi_x^r(1 - H(u))) \cdot (u - U), \\ L_{2,1}(g) &= a_2 \cdot v, \\ L_{2,2}(g) &= -2\alpha_{2,m}\lambda\Phi_y \cdot (v - V). \end{aligned} \tag{B1}$$

To keep the balance in the normal direction of a cell interface, three cases need to be considered,

1. $\psi_1 = 1$

$$\begin{aligned} h\langle L_{1,1}(g)\rangle &= \frac{3}{4}\frac{1}{\sqrt{\pi\lambda}}(h_x^l - h_x^r), \\ h\langle L_{1,2}(g)\rangle &= -\alpha_{1,1}\frac{1}{\sqrt{\pi\lambda}}(h_x^l - h_x^r). \\ \alpha_{1,1} &= 3/4 \end{aligned} \tag{B2}$$

2. $\psi_2 = u^1$

$$\begin{aligned} h\langle L_{1,1}(g)u\rangle &= \frac{1}{2\lambda}(h_x^l + h_x^r), \\ h\langle L_{1,2}(g)u\rangle &= -\alpha_{1,2}\frac{1}{2\lambda}(h_x^l + h_x^r). \\ \alpha_{1,2} &= 1 \end{aligned} \tag{B3}$$

3. $\psi_3 = u^2$

$$\begin{aligned} h\langle L_{1,1}(g)(u^2)\rangle &= \frac{5}{4\lambda\sqrt{\pi\lambda}}(h_x^l - h_x^r), \\ h\langle L_{1,2}(g)(u^2)\rangle &= -\alpha_{1,3}\frac{1}{\lambda\sqrt{\pi\lambda}}(h_x^l - h_x^r). \\ \alpha_{1,3} &= 5/4 \end{aligned} \tag{B4}$$

In the tangential direction of a cell interface, $L_{2,1}(g)$ and $L_{2,2}(g)$ can be naturally balanced by $\alpha_{2,m} = 1$.

APPENDIX C: DERIVATIVES OF EQUILIBRIUM DISTRIBUTION FUNCTION FOR SCALAR TRANSPORT EQUATION

For the scalar transport equation, the first-order spatial and temporal derivatives of equilibrium distribution need to be evaluated. The equilibrium distribution g^s is defined in Eq. (26), which is rewritten as

$$\begin{aligned} g^s &= h\left(\frac{\lambda}{\pi}\right)^{3/2} e^{-\lambda((\mathbf{u}-\mathbf{U})^2+(z-Z)^2)} \\ &= \left(\frac{\lambda}{\pi}\right)^{1/2} e^{-\lambda(z-Z)^2} \cdot h\left(\frac{\lambda}{\pi}\right) e^{-\lambda(\mathbf{u}-\mathbf{U})^2} \\ &= g_1 g, \end{aligned}$$

where $g_1 = (\lambda/\pi)^{1/2} e^{-\lambda(z-Z)^2}$ and $g = h(\lambda/\pi)e^{-\lambda(\mathbf{u}-\mathbf{U})^2}$. The derivative of g^s can be evaluated as

$$\begin{aligned} \frac{\partial g^s}{\partial w} &= \frac{\partial g_1}{\partial w} g + g_1 \frac{\partial g}{\partial w} \\ &= g^s\left[(b_{k,1} + b_{k,2}z + b_{k,3}z^2) \right. \\ &\quad \left. + (a_{k,1} + a_{k,2}u + a_{k,3}v + a_{k,4}(u^2 + v^2))\right], \end{aligned}$$

where w can be x, y, or t. The coefficients $b_{k,m}$ are

$$\begin{aligned} b_{k,1} &= \frac{1}{2}(6\lambda Z^2 - 1)\frac{h_w}{h} - 2\lambda Z\frac{(hZ)_w}{h}, \\ b_{k,2} &= 2\lambda\left(\frac{(hZ)_w}{h} - 2Z\frac{h_w}{h}\right), \\ b_{k,3} &= \lambda\frac{h_w}{h}, \end{aligned} \tag{C1}$$

which are related to the derivatives of macroscopic variables (h, hZ) only.

In GKS with scalar transport, the equilibrium distribution function $\bar{g}^s$ and its derivative $\bar{g}_w^s$ at cell interface have to be fully determined. Besides the determination of $\bar{g}$ in Sec. II, the scalar variable hZ and its derivatives in its equilibrium state $\bar{g}_1$ need to be determined as well from the colliding particles from the left and right sides of the cell interface. The detailed formulas are given as follows:

$$\begin{aligned} (hZ)^e &\equiv \int_{\mathbf{u}}\int_z \bar{g}^s z\mathrm{d}z\mathrm{d}\mathbf{u} \\ &= (hZ)^l\langle u^0\rangle_{u>0} + (hZ)^r\langle u^0\rangle_{u<0} \\ (hZ)_w^e &\equiv \int_{\mathbf{u}}\int_z \bar{g}_w^s z\mathrm{d}z\mathrm{d}\mathbf{u} \\ &= h^l(\langle b_k^l z\rangle_{u>0}\langle u^0\rangle_{u>0} + \langle z\rangle_{u>0}\langle a_k^l\rangle_{u>0}), \\ &\quad + h^r(\langle b_k^r z\rangle_{u<0}\langle u^0\rangle_{u<0} + \langle z\rangle_{u\langle 0}\langle a_k^r\rangle_{u<0}). \end{aligned}$$

The flux for scalar transport is related to a combination of the moments $\langle a^s z u^m v^n\rangle$ at the cell interface, which can be evaluated as

$$\langle a^s z u^m v^n\rangle = \langle b_k z\rangle\langle u^m v^n\rangle + \langle z\rangle\langle a_k u^m v^n\rangle,$$

where $\langle a_k u^m v^n\rangle$ have been obtained already in solving the purely shallow water equations. In summary, for the shallow water equations with scalar transport, the fluxes for (h, hU, and hV) can be evaluated in the same way as that presented in Sec. II. However, for the fluxes of hZ in Eq. (27), the above-defined equilibrium state g^s should be used to get the corresponding f^s in Eq. (28) for the flux evaluations $hZU = \int uzf^s dudvdz$ and $hZV = \int vzf^s dudvdz$.

DATA AVAILABILITY

The data that support the findings of this study are available from the corresponding author upon reasonable request.

REFERENCES

[1]R. J. LeVeque, "Balancing source terms and flux gradients in high-resolution Godunov methods: The quasi-steady wave-propagation algorithm," J. Comput. Phys. **146**(1), 346–365 (1998).
[2]J. G. Zhou, D. M. Causon, C. G. Mingham, and D. M. Ingram, "The surface gradient method for the treatment of source terms in the shallow-water equations," J. Comput. Phys. **168**(1), 1–25 (2001).

[3]K. Xu, "A well-balanced gas-kinetic scheme for the shallow-water equations with source terms," J. Comput. Phys. **178**(2), 533–562 (2002).
[4]D. Wirasaet, E. J. Kubatko, C. E. Michoski, S. Tanaka, J. J. Westerink, and C. Dawson, "Discontinuous Galerkin methods with nodal and hybrid modal/nodal triangular, quadrilateral, and polygonal elements for nonlinear shallow water flow," Comput. Methods Appl. Mech. Eng. **270**, 113–149 (2014).
[5]Z. J. Wang, "High-order methods for the Euler and Navier–Stokes equations on unstructured grids," Prog. Aerosp. Sci. **43**(1–3), 1–41 (2007).
[6]M. Alhawwary and Z. J. Wang, "On the mesh resolution of industrial LES based on the DNS of flow over the T106C turbine," Adv. Aerodyn. **1**(1), 1–18 (2019).
[7]Z. J. Wang and E. Jourdan, "Benchmark for scale-resolving simulation with curved walls: The Taylor Couette flow," Adv. Aerodyn. **3**(1), 1–18 (2021).
[8]Y. Xing and C.-W. Shu, "High order finite difference WENO schemes with the exact conservation property for the shallow water equations," J. Comput. Phys. **208**(1), 206–227 (2005).
[9]Y. Xing and C.-W. Shu, "High order well-balanced finite volume WENO schemes and discontinuous Galerkin methods for a class of hyperbolic systems with source terms," J. Comput. Phys. **214**(2), 567–598 (2006).
[10]M. Ricchiuto, R. Abgrall, and H. Deconinck, "Application of conservative residual distribution schemes to the solution of the shallow water equations on unstructured meshes," J. Comput. Phys. **222**(1), 287–331 (2007).
[11]G. Li, J. Li, S. Qian, and J. Gao, "A well-balanced ADER discontinuous Galerkin method based on differential transformation procedure for shallow water equations," Appl. Math. Comput. **395**, 125848 (2021).
[12]M. Dumbser and M. Käser, "Arbitrary high order non-oscillatory finite volume schemes on unstructured meshes for linear hyperbolic systems," J. Comput. Phys. **221**(2), 693–723 (2007).
[13]S. R. Brus, D. Wirasaet, E. J. Kubatko, J. J. Westerink, and C. Dawson, "High-order discontinuous Galerkin methods for coastal hydrodynamics applications," Comput. Methods Appl. Mech. Eng. **355**, 860–899 (2019).
[14]B. Cockburn and C.-W. Shu, "The Runge–Kutta discontinuous Galerkin method for conservation laws V: Multidimensional systems," J. Comput. Phys. **141**(2), 199–224 (1998).
[15]Z. J. Wang and H. Gao, "A unifying lifting collocation penalty formulation including the discontinuous Galerkin, spectral volume/difference methods for conservation laws on mixed grids," J. Comput. Phys. **228**(21), 8161–8186 (2009).
[16]F. Zhao, X. Ji, W. Shyy, and K. Xu, "A compact high-order gas-kinetic scheme on unstructured mesh for acoustic and shock wave computations," preprint arXiv:2010.05717 (2020).
[17]J. Qiu and C.-W. Shu, "Hermite WENO schemes and their application as limiters for Runge–Kutta discontinuous Galerkin method: One-dimensional case," J. Comput. Phys. **193**(1), 115–135 (2004).
[18]J. Qiu and C.-W. Shu, "Hermite WENO schemes and their application as limiters for Runge–Kutta discontinuous Galerkin method II: Two dimensional case," Comput. Fluids **34**(6), 642–663 (2005).
[19]J. Zhu and J. Qiu, "Hermite WENO schemes and their application as limiters for Runge-Kutta discontinuous Galerkin method, III: Unstructured meshes," J. Sci. Comput. **39**(2), 293–321 (2009).
[20]C.-W. Shu, "High order WENO and DG methods for time-dependent convection-dominated PDEs: A brief survey of several recent developments," J. Comput. Phys. **316**, 598–613 (2016).
[21]K. Xu and K. H. Prendergast, "Numerical navier-stokes solutions from gas kinetic theory," J. Comput. Phys. **114**(1), 9–17 (1994).
[22]K. Xu, "Gas-kinetic schemes for unsteady compressible flow simulations," in *The 29th Computational Fluid Dynamics, VKI Lecture Series, Von Karman Institute for Fluid Dynamics*, Rhode-St-Genèse, Belgium (von Karman Institute, 1998), pp. 1–202.
[23]K. Xu, "A gas-kinetic BGK scheme for the Navier–Stokes equations and its connection with artificial dissipation and Godunov method," J. Comput. Phys. **171**(1), 289–335 (2001).
[24]X. Kun, *Direct Modeling for Computational Fluid Dynamics: Construction and Application of Unified Gas-Kinetic Schemes* (World Scientific, 2015).
[25]G. Cao, H. Liu, and K. Xu, "Physical modeling and numerical studies of three-dimensional non-equilibrium multi-temperature flows," Phys. Fluids **30**(12), 126104 (2018).
[26]C. Liu and K. Xu, "Unified gas-kinetic wave-particle methods IV: Multi-species gas mixture and plasma transport," Adv. Aerodyn. **3**(1), 1–31 (2021).
[27]Y. Zhu, C. Liu, C. Zhong, and K. Xu, "Unified gas-kinetic wave-particle methods. II. Multiscale simulation on unstructured mesh," Phys. Fluids **31**(6), 067105 (2019).
[28]Y. Chen, Y. Zhu, and K. Xu, "A three-dimensional unified gas-kinetic wave-particle solver for flow computation in all regimes," Phys. Fluids **32**(9), 096108 (2020).
[29]F. Zhao, X. Ji, W. Shyy, and K. Xu, "Direct modeling for computational fluid dynamics and the construction of high-order compact scheme for compressible flow simulations," preprint arXiv:2107.06555 (2021).
[30]A. Harten, B. Engquist, S. Osher, and S. R. Chakravarthy, "Uniformly high order accurate essentially non-oscillatory schemes, III," J. Comput. Phys. **71**(2), 231–303 (1987).
[31]X.-D. Liu, S. Osher, and T. Chan, "Weighted essentially non-oscillatory schemes," J. Comput. Phys. **115**(1), 200–212 (1994).
[32]A. K. Henrick, T. D. Aslam, and J. M. Powers, "Mapped weighted essentially non-oscillatory schemes: Achieving optimal order near critical points," J. Comput. Phys. **207**(2), 542–567 (2005).
[33]R. Borges, M. Carmona, B. Costa, and W. Sun Don, "An improved weighted essentially non-oscillatory scheme for hyperbolic conservation laws," J. Comput. Phys. **227**(6), 3191–3211 (2008).
[34]F. Zhao, L. Pan, Z. Li, and S. Wang, "A new class of high-order weighted essentially non-oscillatory schemes for hyperbolic conservation laws," Comput. Fluids **159**, 81–94 (2017).
[35]C.-W. Shu, "High order weighted essentially nonoscillatory schemes for convection dominated problems," SIAM Rev. **51**(1), 82–126 (2009).
[36]C. Hu and C.-W. Shu, "Weighted essentially non-oscillatory schemes on triangular meshes," J. Comput. Phys. **150**(1), 97–127 (1999).
[37]F. Zhao, L. Pan, and S. Wang, "Weighted essentially non-oscillatory scheme on unstructured quadrilateral and triangular meshes for hyperbolic conservation laws," J. Comput. Phys. **374**, 605–624 (2018).
[38]G.-S. Jiang and C.-W. Shu, "Efficient implementation of weighted ENO schemes," J. Comput. Phys. **126**(1), 202–228 (1996).
[39]J. Li and Z. Du, "A two-stage fourth order time-accurate discretization for Lax–Wendroff type flow solvers I. Hyperbolic conservation laws," SIAM J. Sci. Comput. **38**(5), A3046–A3069 (2016).
[40]J. Li, "Two-stage fourth order: Temporal-spatial coupling in computational fluid dynamics (CFD)," Adv. Aerodyn. **1**, 1–36 (2019).
[41]L. Pan, K. Xu, Q. Li, and J. Li, "An efficient and accurate two-stage fourth-order gas-kinetic scheme for the Euler and Navier–Stokes equations," J. Comput. Phys. **326**, 197–221 (2016).
[42]L. Pan, J. Cheng, S. Wang, and K. Xu, "A two-stage fourth-order gas-kinetic scheme for compressible multicomponent flows," Commun. Comput. Phys. **22**(4), 1123–1149 (2017).
[43]X. Ji, F. Zhao, W. Shyy, and K. Xu, "A family of high-order gas-kinetic schemes and its comparison with Riemann solver based high-order methods," J. Comput. Phys. **356**, 150–173 (2018).
[44]X. Ji, L. Pan, W. Shyy, and K. Xu, "A compact fourth-order gas-kinetic scheme for the Euler and Navier–Stokes equations," J. Comput. Phys. **372**, 446–472 (2018).
[45]D. C. Seal, Y. Güçlü, and A. J. Christlieb, "High-order multiderivative time integrators for hyperbolic conservation laws," J. Sci. Comput. **60**(1), 101–140 (2014).
[46]F. Zhao, X. Ji, W. Shyy, and K. Xu, "Compact higher-order gas-kinetic schemes with spectral-like resolution for compressible flow simulations," Adv. Aerodyn. **1**, 13 (2019).
[47]C. G. Mingham and D. M. Causon, "High-resolution finite-volume method for shallow water flows," J. Hydraul. Eng. **124**(6), 605–614 (1998).
[48]P. García-Navarro, J. Murillo, J. Fernández-Pato, I. Echeverribar, and M. Morales-Hernández, "The shallow water equations and their application to realistic cases," Environ. Fluid Mech. **19**(5), 1235–1252 (2019).

[49]K. Kazhyken, J. Videman, and C. Dawson, "Discontinuous Galerkin methods for a dispersive wave hydro-morphodynamic model with bed-load transport," Comput. Methods Appl. Mech. Eng. **375**, 113592 (2021).
[50]M. Iervolino, A. Leopardi, S. Soares-Frazão, C. Swartenbroekx, and Y. Zech "2D-H numerical simulation of dam-break flow on mobile bed with sudden enlargement," River Flow **2010**, 569–576.
[51]L. Goutiere, S. Soares-Frazão, and Y. Zech, "Dam-break flow on mobile bed in abruptly widening channel: Experimental data," J. Hydraul. Res. **49**(3), 367–371 (2011).
[52]X. Liu, A. Mohammadian, and J. Á. Infante Sedano, "A numerical model for three-dimensional shallow water flows with sharp gradients over mobile topography," Comput. Fluids **154**, 1–11 (2017).